

See discussions, stats, and author profiles for this publication at: <https://www.researchgate.net/publication/263953832>

Au@ZIFs: Stabilization and Encapsulation of Cavity-Size Matching Gold Clusters inside Functionalized Zeolite Imidazolate Frameworks, ZIFs

ARTICLE *in* CHEMISTRY OF MATERIALS · NOVEMBER 2010

Impact Factor: 8.35 · DOI: 10.1021/cm102529c

CITATIONS

96

READS

135

5 AUTHORS, INCLUDING:



Stuart Turner

University of Antwerp

170 PUBLICATIONS **1,757** CITATIONS

SEE PROFILE



Oleg I Lebedev

National Graduate School of Engineering an...

370 PUBLICATIONS **5,240** CITATIONS

SEE PROFILE

Au@ZIFs: Stabilization and Encapsulation of Cavity-Size Matching Gold Clusters inside Functionalized Zeolite Imidazolate Frameworks, ZIFs

Daniel Esken,[†] Stuart Turner,[‡] Oleg I. Lebedev,[§] Gustaaf Van Tendeloo,[‡] and Roland A. Fischer^{*,†}

[†]*Inorganic Chemistry II, Ruhr-University Bochum, Universitätsstrasse 150, 44801 Bochum, Germany,*

[‡]*EMAT, University of Antwerp, Groenenborgerlaan 171, 2020 Antwerp, Belgium, and* [§]*Laboratoire CRISMAT, UMR 6508, CNRS-ENSICAEN, 6 Bd du Maréchal Juin, F-14050 Caen, France*

Received September 3, 2010. Revised Manuscript Received October 20, 2010

The selective formation and stabilization of very small, naked metal particles inside the cavities of metal–organic frameworks (MOFs) and the simultaneous realization of an even distribution of the particles throughout the crystalline MOF host matrix over a wide range of metal loading are challenging goals. MOFs reveal high specific surface areas, tunable pore sizes, and organic linkers, which are able to interact with guests. The chemically very robust zeolite imidazolate frameworks (ZIFs) are a subclass of MOFs. We chose the microporous sodalite-like ZIF-8 ($\text{Zn}(\text{MeIM})_2$; IM = imidazolate) and ZIF-90 ($\text{Zn}(\text{ICA})_2$; ICA = imidazolate-2-carboxyaldehyde) as host matrices to influence the dispersion of imbedded gold nanoparticles (Au NPs). The metal loading was achieved via gas phase infiltration of $[\text{Au}(\text{CO})\text{Cl}]$ followed by a thermal hydrogenation step to form the Au NPs. Low-dose high-resolution transmission electron microscopy ((HR)TEM) and electron tomography reveal a homogeneous distribution of Au NPs throughout the ZIF matrix. The functional groups of ZIF-90 direct the anchoring of intermediate Au species and stabilize drastically smaller and quite monodisperse Au NPs in contrast to the parent not functionalized ZIF-8. The particles can be very small, match the cavity size and approach defined molecular clusters of magic numbers, i.e., Au_{55} , independently from the level of loading. Post-synthetic oxidation of the aldehyde groups to yield alkyl esters by the adjacent, catalytically active metal NPs is presented as a new concept of encapsulating nanoparticles inside MOFs and allows multiple steps of metal loadings without decomposition of the MOF.

Introduction

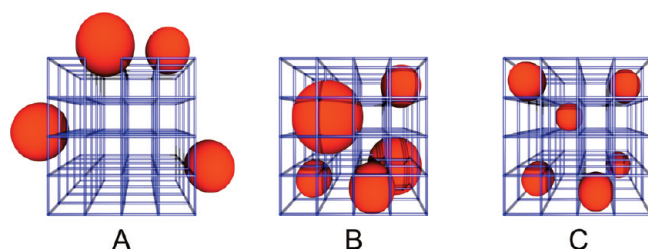
The chemistry of porous, crystalline coordination polymers (PCPs), also called metal–organic frameworks (MOFs), has captured widespread attention on the way to important large-scale industrial applications such as gas storage,¹ gas separation,² and catalysis.³ These novel hybrid inorganic–organic solid-state compounds are formed by the linking of single metal ions or multinuclear metal ion building units with appropriate oligotopic organic ligands. A guideline for MOF synthesis and a library of possible structures is given by the principles and the know how of established metal–organic coordination chemistry combined with

the topology of augmented periodic networks (“reticular chemistry”).⁴ Tailored functionalizing of the coordination space of MOFs offers unique perspectives that are beyond any other porous materials. In addition to the modification of the framework itself,⁵ the host–guest chemistry of MOFs allows the implementation of desired properties by filling the cavities with guest molecules and clusters.^{6,7} In particular, the doping of MOFs with metal nanoparticles (NPs) is of interest for heterogeneous catalysis⁸ and hydrogen storage.^{9,10} An important aspect on the deposition of metals at MOFs is the question whether the NPs are distributed evenly over the volume of the MOF crystallite with a size dispersion matching with the dimensions of the channels or cavities or if

*Corresponding author. E-mail: roland.fischer@rub.de.

- (1) Czaja, A. U.; Trukhan, N.; Müller, U. *Chem. Soc. Rev.* **2009**, *38*, 1284–1293.
- (2) Li, J.-R.; Kuppler, R. J.; Zhou, H.-C. *Chem. Soc. Rev.* **2009**, *38*, 1477–1504.
- (3) Lee, J. Y.; Farha, O. K.; Roberts, J.; Scheidt, K. A.; Nguyen, S. T.; Hupp, J. T. *Chem. Soc. Rev.* **2009**, *38*, 1450–1459. Farrusseng, D.; Aguado, S.; Pinel, C. *Angew. Chem., Int. Ed.* **2009**, *48*, 7502–7513. Chizallet, C.; Lazare, S.; Bazer-Bachi, D.; Bonnier, F.; Lecocq, V.; Soyer, E.; Quoineaud, A.; Bats, N. *J. Am. Chem. Soc.* **2010**, *132*, 12365–12377.
- (4) Delgado-Friedrichs, O.; O’Keeffe, M.; Yaghi, O. M. *Phys. Chem. Chem. Phys.* **2007**, *9*, 1035–1042.

- (5) Wang, Z.; Cohen, S. M. *Chem. Soc. Rev.* **2009**, *38*, 1315–1329.
- (6) Halder, G. J.; Kepert, C. J.; Moubaraki, B.; Murray, K. S.; Cashion, J. D. *Science* **2002**, *298*, 1762–1765.
- (7) Maksimchuk, N. V.; Timofeeva, M. N.; Melgunov, M. S.; Shmakov, A. N.; Chesalov, Y. A.; Dybtsev, D. N.; Fedin, V. P.; Kholdeeva, O. A. *J. Catal.* **2008**, *257*, 315–323.
- (8) Corma, A.; H. Garcia, H.; Llabres i Xamena, F. X. *Chem. Rev.* **110**, DOI 10.1021/cr9003924 (2010).
- (9) Zlotea, C.; Campesi, R.; Cuevas, F.; Leroy, E.; Dibandjo, P.; Volklinger, C.; Loiseau, T.; Férey, G.; Latroche, M. *J. Am. Chem. Soc.* **2010**, *132*, 2991–2997.
- (10) Cheon, Y. E.; Suh, M. P. *Angew. Chem., Int. Ed.* **2009**, *48*, 2899–2903.

Scheme 1. Three Characteristic Cases A, B, and C of Microstructures for Nanoparticles Supported by Metal-Organic Frameworks^a

^a(A) Particles typically larger than cavity size with a preferred anchoring close to the outer surface of the MOF. (B) Particles evenly distributed throughout the volume of the MOF crystal but still exhibiting a broad size distribution with an average particle size exceeding the dimensions of the pores. (C) Particles with a narrow size distribution matching with the cavities and homogeneously distributed over the volume of MOF. The real microstructure may be more or less close to one of these conceptual limiting cases. If particle sizes are, however, larger than the typical pore dimensions as for A and B local damage of the MOF support matrix has to be taken into account, which is not shown in the scheme.

the particles accumulate preferentially at the outer surface regions of the MOF with a pronounced tendency to exceed the pore size substantially (Scheme 1). The former case may be called “metals@MOF” (or “metals⊃MOFs”).^{11,12} The abbreviation “@” (or “⊃”) emphasizes the preferred inclusion of the particles inside the cavities throughout the MOF volume (Scheme 1B, C), whereas deposition preferentially close or at the outer surfaces of the MOF crystallites may be better written as “metals/MOFs” as this is the notation for supported nano materials (e.g., catalysts) in general (Scheme 1A). There might be a substantial local damage of the MOF support matrix if the particle sizes are significantly larger than the typical pore dimensions (cases A, B). The limiting case is situation C of cavity size matching particles homogeneously distributed throughout an intact, defect-free crystalline MOF matrix.

The elucidation of the actual microstructure and unambiguous assignment to A, B, or C needs a combination of complementary analytical methods including Transmission Electron Microscopy (TEM). However, MOFs are known to be labile under the electron beam at routine conditions of TEM measurement and high-quality TEM studies combining electron diffraction information of the MOF host with images of the pore structure are very rare. Accordingly, Allendorf and co-workers pointed out that the microstructures of metal@MOF systems obtained by TEM revealing metal NPs typically exceeding the pore size regime may be artifacts caused by the disintegration of the MOF matrix under the electron beam which is accompanied by the growth of the initial metal particles.¹³ This is especially relevant if multiple imaging of the specimen is done in the course of electron tomography to rigorously

asses the spatial distribution of the metal NPs within the bulk of the MOF matrix. Obviously, such TEM studies involving MOF materials are quite sophisticated and must be done with great care and using low-dose techniques to rule out substantial and ill-defined changes of the sample during the measurement.¹⁴

As a matter of fact, evidence of loading a MOF matrix selectively with cavity size matching metal particles unambiguously approaching the limiting microstructure C and stabilizing the particles against further growth has been absent. For example, the solvent-free, gas-phase deposition of Au NPs on [Zn₄O(bdc)₃] (MOF-5) using volatile molecular precursors for Au lead to materials Au/MOF-5 with a broad size distribution of Au particles of 5–20 nm that are largely located outside the MOF matrix with microstructures closer to A than B and not approaching C.¹¹ This segregation effect of Au NPs is also well-known for other weakly interacting supports such as mesoporous silica or carbon materials.¹⁵ Nevertheless, Haruta et al. demonstrated solvent-free deposition of Au NPs at a series of different MOFs and reported on their catalytic properties^{16,17} but, as mentioned above, without much evidence of the microstructures of the particular Au/MOF systems.

We, however, are determined to achieve and study metal@MOF systems that are as close as possible to the ideal case C and ruling out any artifacts associated with TEM imaging. For this purpose, the loading of zeolitic imidazolate frameworks (ZIFs) with Au NPs was selected as the model case. ZIFs exhibit zeolite network topologies, consisting of functionalized imidazolate groups linking tetra-coordinated Zn²⁺ or Co²⁺ metal ions.¹⁸ ZIFs show exceptionally high thermal stability and chemical robustness, which are different for many other MOFs. We chose the microporous ZIF-8 (Zn(MeIM)₂; MeIM = imidazolate-2-methyl; S(N₂) = 1918 m² g⁻¹),¹⁸ and ZIF-90 (Zn(ICA)₂; ICA = imidazolate-2-carboxyaldehyde; S(N₂) = 1664 m² g⁻¹).¹⁹ Both ZIFs exhibit the very same sodalite-like structure with pore sizes of 1.2 nm and quite small pore windows of 3.5 Å. These features should restrain the growth of Au clusters inside the cavities of the ZIF matrix by steric effects. The only differences between the ZIFs are the methyl vs the aldehyde functions at the linkers. Thus, the matrices of identical topology are nevertheless very likely to interact differently with the adsorbed gold precursor molecule, the intermediate Au species and the final Au clusters formed in the course of the hydrogenation step of [Au(CO)Cl]@ZIF. According to high resolution transmission electron microscopy (HRTEM),

- (11) Hermes, S.; Schröter, M. K.; Schmid, R.; Khodeir, L.; Muhler, M.; Tissler, A.; Fischer, R. W.; Fischer, R. A. *Angew. Chem., Int. Ed.* **2005**, *44*, 6237–6241.
- (12) Schröder, F.; Esken, D.; Cokoja, M.; van den Berg, M.; Lebedev, O. I.; Tendelo, G.; Walaszek, B.; Buntkowsky, G.; Limbach, H.; Chaudret, B.; Fischer, R. A. *J. Am. Chem. Soc.* **2008**, *130*, 6119–6130.
- (13) Houk, R. J. T.; Jacobs, B. W.; El Gabaly, F.; Chang, N. N.; Talin, A. A.; Graham, D. D.; House, S. D.; Robertson, I. M.; Allendorf, M. D. *Nano Lett.* **2009**, *9*, 3413–3418.

- (14) Turner, S.; Lebedev, O. I.; Schröder, F.; Esken, D.; Fischer, R. A.; Van Tendeloo, G. *Chem. Mater.* **2008**, *20*, 5622–5627.
- (15) Tsung, C.-K.; Hong, W.; Shi, Q.; Kou, X.; Yeung, M. H.; Wang, J.; Stucky, G. D. *Adv. Funct. Mater.* **2006**, *16*, 2225–2230.
- (16) Ishida, T.; Nagaoka, M.; Akita, T.; Haruta, M. *Chem.—Eur. J.* **2008**, *14*, 8456–8460.
- (17) Jiang, H.-L.; Liu, B.; Akita, T.; Haruta, M.; Sakurai, H.; Xu, Q. *J. Am. Chem. Soc.* **2009**, *131*, 11302–11303.
- (18) Park, K. S.; Ni, Z.; Côté, A. P.; Choi, J. Y.; Huang, R.; Uribe-Romo, F. J.; Chae, H. K.; O’Keeffe, M.; Yaghi, O. M. *Proc. Natl. Acad. Sci. U.S.A.* **2006**, *103*, 10186–10191.
- (19) Morris, W.; Doonan, C. J.; Furukawa, H.; Banerjee, R.; Yaghi, O. M. *J. Am. Chem. Soc.* **2008**, *130*, 12626–12627.

electron tomography (ET) and UV–vis spectroscopy the obtained material Au@ZIF-90 turned out to be the first unambiguous case of cavity size matched, very small Au clusters homogeneously dispersed and stabilized inside a crystalline and intact MOF matrix. The aldehyde groups act as anchors for gold species and restrained the growth and control the size dispersion of the particles much more effectively as compared with the nonfunctionalized and less interacting ZIF-8.

Results and Discussion

Gas phase infiltration of the volatile, small, and rod-shaped gold complex $[\text{Au}(\text{CO})\text{Cl}]$ into the activated ZIFs and the subsequent hydrogenation of the obtained $[\text{Au}(\text{CO})\text{Cl}]\text{@ZIF}$ materials at 100–130 °C and 2 bar H_2 over a few hours in order to release CO and HCl yield the samples Au@ZIF summarized in Table 1. The obtained Au content can be controlled by the molar ratios of ZIF and $[\text{Au}(\text{CO})\text{Cl}]$ during the infiltration process. The loading was varied between 5 and 30 wt.% (i.e., up to 33 mol %) by employing a single loading step (Table 1). The resulting BET surface areas obtained by standard nitrogen adsorption studies are between 1334 and 787 $\text{m}^2 \text{g}^{-1}$ for Au@ZIF-8 (**1**; 10 and 30 wt % Au) and 1004 and 632 $\text{m}^2 \text{g}^{-1}$ for Au@ZIF-90 (**2**; 10 and 30 wt % Au). These values and the inspection of the isotherms (Type I) of the loaded materials in comparison with the parent, activated ZIFs indicate that the pores are accessible and not substantially blocked with gold particles at or close to the outer surface of the matrix. In addition, significant contributions of mesoporosity can safely be ruled out. Accordingly, the PXRD data (Figure 1) reveal fully intact framework structures after the incorporation of gold. Neither the peak positions nor the line shapes were changed significantly. Only the intensity ratio of the (110) reflex to the (200) reflex of the gold loaded ZIF materials in comparison to guest-free ZIF is decreased a little, which gives evidence for some pore filling.^{12,20} A weak Au (111) reflex at $38.1^\circ 2\theta$ is observed for **1** (5 and 30 wt.% Au) which is assigned to gold nanoparticles of an average size of $3.2 (\pm 0.1) \text{ nm}$ based on single peak profile analysis. This reflex is absent or too broad and too weak to be observed in case of **2** (5 and 30 wt % Au), which indicates small particles well below 2 nm. Accordingly, the UV–vis spectra of **1** show a pronounced plasmon resonance peak at 518 nm, quite matching with solution stabilized Au NPs in perfluorodecanethiol with diameters of 1.5 to 5.4 nm.²¹ The significant broadening and the blue shift to 508 nm of the surface plasmon band for **2** substantiates the assignment of Au NPs $\leq 1.5 \text{ nm}$ (see Figure S18 in the Supporting Information).^{22,23} This remarkable difference between ZIF-8 and ZIF-90 as host

Table 1. Elemental Analysis of the Gold Loaded ZIF Samples

composite material	gold amount (wt %)	C (wt %)	H (wt %)	N (wt %)	Zn (wt %)	Au (wt %)
Au@ZIF-8	30	28.9	2.8	16.8	20.7	29.6
Au@ZIF-8	10	37.5	3.5	21.8	25.5	10.3
Au@ZIF-8	5	39.4	3.9	22.6	27.2	5.4
Au@ZIF-90	30	25.5	1.6	15.1	17.5	29.5
Au@ZIF-90	10	32.2	2.1	19.2	22.9	9.8
Au@ZIF-90	5	35.1	2.2	20.5	23.7	5.2

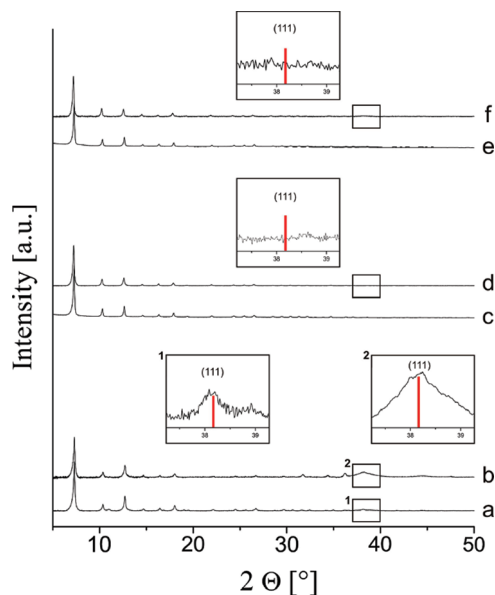


Figure 1. Comparison of the powder X-ray diffraction patterns of Au@ZIF samples obtained by a one step loading with Au NPs: (a) Au_{5 wt %}@ZIF-8, (b) Au_{30 wt %}@ZIF-8, (c) Au_{5 wt %}@ZIF-90, (d) Au_{30 wt %}@ZIF-90, (e) Au_{5 wt %}@ZIF-90(ox), and (f) Au_{30 wt %}@ZIF-90(ox); (red line: [111] Au reflex, JPDFS reference no. 001–1172).

matrices for the Au NPs is attributed to the efficient anchoring of AuCl species at the aldehyde function of ZIF-90 in the course of releasing the very labile bonded CO ligand as seen in the corresponding FT-IR spectra of the precursor loaded ZIFs before hydrogenation. However, direct evidence for the suggested cluster stabilizing $-\text{CHO} \cdots \text{Au}$ interaction after hydrogenation could neither be extracted from the FTIR nor from the solid-state NMR spectra of **2** (see the Supporting Information).

High-resolution TEM imaging of **1** gives evidence for Au NPs with a broad size distribution of 1–5 nm. Note, that TEM, PXRD and UV–vis data on the particle size dispersion are congruent in our case, which rules out substantial particle growth caused by TEM imaging. The bright-field TEM image (Figure 2) show an even size distribution of the Au NPs. The majority of the particles are about 2–4 times larger than the dimensions of the ZIF-8 cavity (1.2 nm) but appear to be rounded, as if they are nevertheless adapted to the shape of the cage. Some particles exhibit no defects while others have a decahedral (5-fold twinning) or icosahedral morphology (2, 3, and 5 fold twinning). Both morphologies are typical for gold nanoparticles of that size regime.²⁴ Particle sizes somewhat exceeding the characteristic dimension of the MOF

(20) Hafizovic, J.; Bjorgen, M.; Olsbye, U.; Dietzel, P. D. C.; Bordiga, S.; Prestipino, C.; Lamberti, C.; Lillerud, K. P. *J. Am. Chem. Soc.* **2007**, *129*, 3612–3620.

(21) Yonezawa, T.; Onoue, S.; Kimizuka, N. *Langmuir* **2001**, *17*, 2291–2293.

(22) Fauth, K.; Kreibitz, U.; Schmid, G. Z. *Phys. D* **1989**, *12*, 515–520.

(23) Rapoport, D. H.; Vogel, W.; Cölfen, H.; Schlögl, R. *J. Phys. Chem. B* **1997**, *101*, 4176–4183.

(24) Ino, S. *J. Phys. Soc. Jpn.* **1966**, *21*, 346–362.

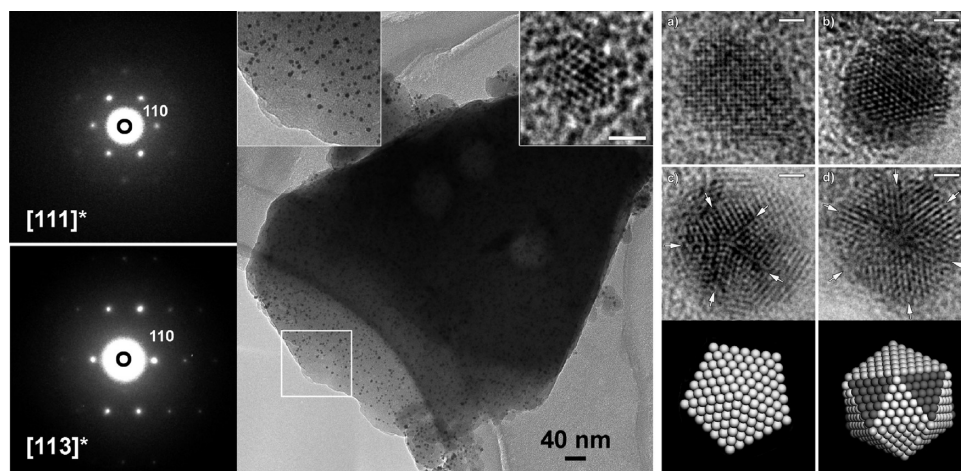


Figure 2. Low magnification TEM of an Au@ZIF-8 crystal (30 wt.% Au). (Center) Bright-field TEM image of a large ZIF-8 crystal loaded with Au NPs with sizes ranging from 1–5 nm. Left inset: magnified image of the area indicated in the center showing the distribution of the Au nanoparticles. Right inset: HRTEM image of a 1.2 nm truncated octahedral Au NP imaged in [110] zone axis. The indicated scale bar is 1 nm. (Left) Electron diffraction patterns taken from typical ZIF-8 crystals in [111] and [113] zone axis evidencing the cubic crystal structure of the ZIF-8 matrix. (Right) High Resolution TEM images of Au NPs: a) Rounded Au nanoparticle imaged along the [001] zone axis. b) Rounded Au NP imaged along the [110] zone axis. c) Decahedral Au NP together with an atomic model imaged along its five-fold symmetry axis. The five-fold twin structure is indicated by arrows. d) Icosahedral Au NP together with an atomic model imaged along one of its three-fold symmetry axis. The symmetry is indicated by arrows. The indicated scale bars are 1 nm.

cavities are typically observed for metal/MOF materials and were attributed to local defects or deformations of the host framework, similar to the situation of metal particle loaded zeolites, but these local defects are usually not affecting the overall structural integrity of the MOF.^{12,25} Note, that at the highest loading level of 30 wt % only 1.2% of the pores are filled with Au NPs, assuming that a 3.2 nm large nanoparticle occupies 4 ZIF cavities.

The stabilization of small Au NPs by weakly interacting matrices or support materials such as MOFs is difficult as pointed out in the introduction. Au NPs are particularly mobile and tend to diffuse outside the channels and cavities of highly porous matrices as it is known for Au/MCM and Au/porous carbon.^{26,27} To unambiguously characterize the distribution of the nanoparticles within the ZIFs as matrix, we have used electron tomography (Figure 3). A slice through a reconstructed Au@ZIF-8 crystal volume (Figure 3b) clearly shows that the Au NPs are evenly spread throughout the ZIF matrix. The 3D rendered volume in Figure 3c shows the distribution as well as the edges of the imaged specimen of **1** (a movie is attached to the Supporting Information). Thus, we assign **1** to be much closer to situation B than it is to situation A (Scheme 1). This result is quite different from Au/MOF-5 materials, which can exhibit very large Au particles up to 20 nm in size predominantly outside the matrix depending on the deposition method.^{11,16} ZIF-8 is better suited to restrict mobility and particle growth and to stabilize small Au particles inside the volume than other MOFs and particular MOF-5, possibly due to the reduced porosity and much smaller pore windows of ZIF-8.

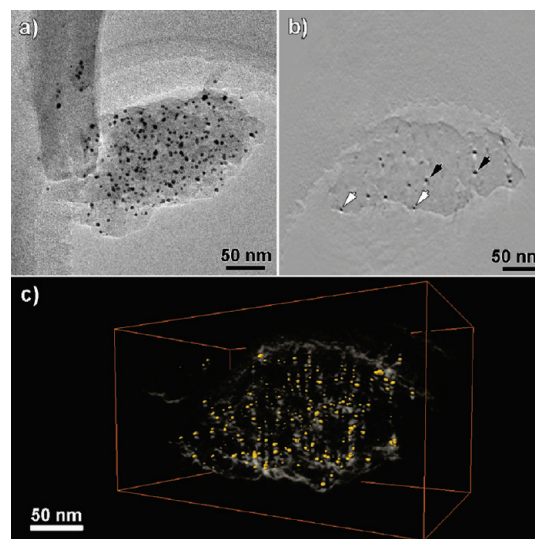


Figure 3. Tomographic reconstruction of Au@ZIF-8 (**1**, 30 wt % Au): (a) Bright-field TEM image of a loaded Au@ZIF-8 crystal. (b) Slice through the tomographically reconstructed volume. The Au NPs are spread evenly throughout the ZIF-8 crystal. Some are positioned at the ZIF-8 surface (white arrows) others are embedded within the ZIF-8 crystal (black arrows). (c) Image of the 3D rendered volume showing the Au NP nanoparticle distribution as well as the edges of the imaged crystal.

Similar TEM studies were done for Au@ZIF-90 (**2**, 5 wt % and 30 wt % Au). Figure 4 displays a bright-field image and a high-angle annular dark field scanning transmission electron microscopy (HAADF-STEM) image of **2** (5 wt.% and 30 wt.% Au). Now, very small particles in the size regime of 1–2 nm are homogeneously spread throughout the specimen. A slice through the tomographically reconstructed volume again clearly confirms the homogeneous three-dimensional distribution of the particles throughout the interior of the ZIF-90 matrix. With a quite narrow size distribution (>95%, ≤2 nm) and a mean diameter of 1.4 (± 0.2) nm the nanoparticles are characteristically smaller than was found for **1** and do much

- (25) Kampers, F. W. H.; Engelen, C. W. R.; Van Hooff, J. H. C.; Koningsberger, D. C. *J. Phys. Chem.* **1990**, *94*, 8574–8578.
- (26) Bandyopadhyay, M.; Korsak, O.; van den Berg, M.; Grünert, W.; Birkner, A.; Li, W.; Schüth, F.; Gies, H. *Microporous Mesoporous Mater.* **2006**, *89*, 158–163.
- (27) Yang, C. M.; Kalwei, M.; Schüth, F.; Chao, K. J. *Appl. Catal., A* **2003**, *254*, 289–296.

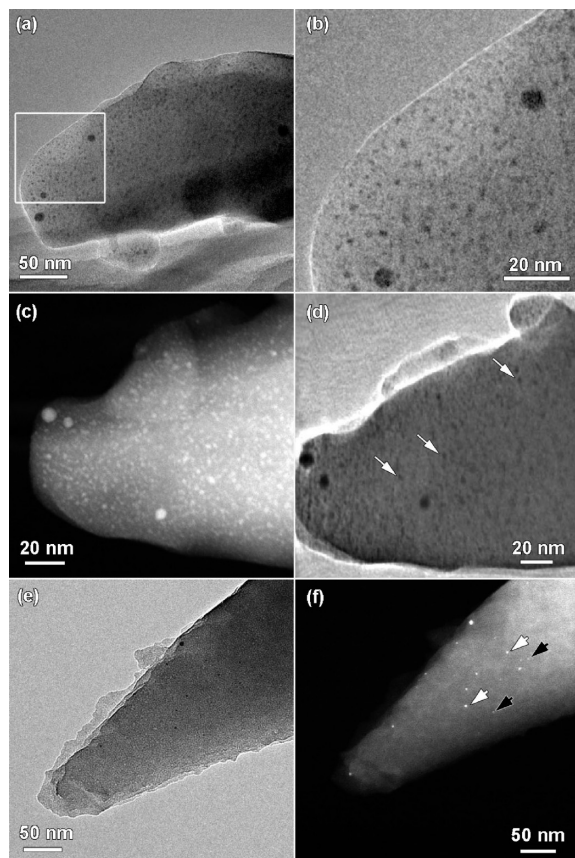


Figure 4. Tomographic reconstruction of Au@ZIF-90 (2, 30 wt % Au): (a) Bright-field TEM image taken at +70° tilt showing the ZIF-90 crystal matrix and small Au NPs embedded within the matrix. (b) Enlarged image of the region indicated in image a. The nanoparticles have a narrow size distribution with an average size around 1–2 nm. (c) HAADF-STEM image showing the same ZIF-90 crystal at 0° tilt. The small nanoparticles are imaged as bright white dots because of the mass–thickness contrast regime in HAADF-STEM. (d) Slice through the tomographically reconstructed volume. Even though the Au particles are very small in the ZIF-90 sample, they can still be distinguished from the ZIF-90 matrix in the tomographic reconstruction. The ZIF-90 matrix is heavily loaded with Au NPs that are clearly inside the matrix, and not positioned preferentially at the surface of the crystal. (e) Bright-field TEM image of a low loaded sample Au@ZIF-90 (2, 5 wt % Au) showing the ZIF-90 crystal matrix and very small gold nanoparticles. (f) HAADF-STEM image showing the same ZIF-90 crystal as in image e. The small Au NPs are imaged as bright white dots and marked with arrows. Particles are as small as in the high loaded sample Au@ZIF-90 (2, 30 wt % Au), indicating that nanoparticle size is independent from the gold amount inside the framework.

better match the size of the cavity of 1.2 nm (Figure 5). Thus, the material clearly approaches the microstructure C. Most interestingly, the size distribution of the Au@ZIF-90 materials was independent from the loading as indicated by the PXRD data (Figure 1) and the corresponding HRTEM of a reference sample of 2 with 5 wt % Au loading (Figure 4). The Au NPs or clusters Au_n of that size regime are known to be icosahedral with particular stable structures at magic numbers n .²³ The expected sizes of Au_n clusters with magic numbers $n = 13, 55, 147$ are 0.84, 1.40, and 1.68 nm, respectively. The TEM data and the blue-shifted UV–vis plasmon resonance support the tentative assignment of the typical gold cluster size inside ZIF-90 comparable to Au_{55} .

Because ZIF-90 exhibits the same network topology and porosity as ZIF-8 the aldehyde- and imidazolate-linkers

must be responsible for the effective stabilization of small Au NPs. In the first place, the surface anchoring of the Au–Cl species at the functional groups, as revealed by FT-IR of the intermediate $[AuCl]@ZIF-90$ for example, is likely to block their mobility which hinders subsequent particle growth during the hydrogenation step. Note, that in case of ZIF-8 as host matrix, the formation of Au particles already starts parallel to the loading, as mentioned above as evidenced by PXRD before the hydrogenation. In addition, we assume a surfactant-like surface capping effect on the Au NPs, which prevents the formation of larger aggregates.

Liquid-phase aerobic catalytic oxidation of benzyl alcohol (BA) to methyl benzoate (MB) was used to probe and compare the surface accessibility of the imbedded Au NPs in 1 and 2. Both benzyl alcohol and the product molecules are able to access the pores of ZIF-8 and ZIF-90 and can diffuse through the network. Loading experiments with BA and MB were conducted and the obtained inclusion compounds were characterized by thermal gravimetric analysis (see Figure S25 in the Supporting Information). Thus, reaction of BA to benzaldehyde, and in presence of MeOH to MB, can take place inside the pore volume of the ZIF matrices at the surface of the caged Au NPs (Scheme 2). The PXRD and TEM data which were taken after the catalysis test reaction showed intact framework structures and still small Au NPs without change of the size distribution, indicating that the host matrices do not change or decompose under the reaction conditions (see Figures S23 and S24 in the Supporting Information).

Au@ZIF-8 exhibits a good conversion of 81% and a high selectivity of 98% (Table 2), matching with Haruta's Au catalysts deposited at MOFs (MOF = MOF-5, MIL-53, CPL-1, CPL-2, HKUST-1).¹⁶ Note, that even Au/MOF-5 with Au NPs of > 5 nm show high performance in liquid phase alcohol oxidation unless the pronounced instability of the MOF-5 support material under the conditions of such reactions with water as stoichiometric byproduct. In sharp contrast to these examples, the material 2 reveals a very weak catalytic activity with a conversion of BA to methyl benzoate of only 13% and a selectivity drop to 50% (Table 2). This effect is caused by the in situ oxidation of the aldehyde functions of ZIF-90 taking place in parallel to the conversion of BA to MB. The intercalated gold nanoparticles catalyze the oxidation of the nearby imidazolate-2-carboxyaldehyde groups to imidazolate-2-methylcarboxylate (IMC) in methanol under oxygen pressure. Note, that metal nanoparticles imbedded into MOFs may very well chemically interact with the organic linkers, as we have shown in detail by H/D exchange processes in case of Ru@MOF-5.¹² Accordingly, benzyl alcohol, benzaldehyde and methyl benzoate molecules are hindered to diffuse through the framework of Au@ZIF-90(ox) and in particular cannot reach or effectively interact with the encapsulated Au NPs inside. We attribute the residual catalyst performance of the material to the quite few and somewhat larger Au NPs deposited close to the outer surface which are likely to be more accessible (Figure 5).

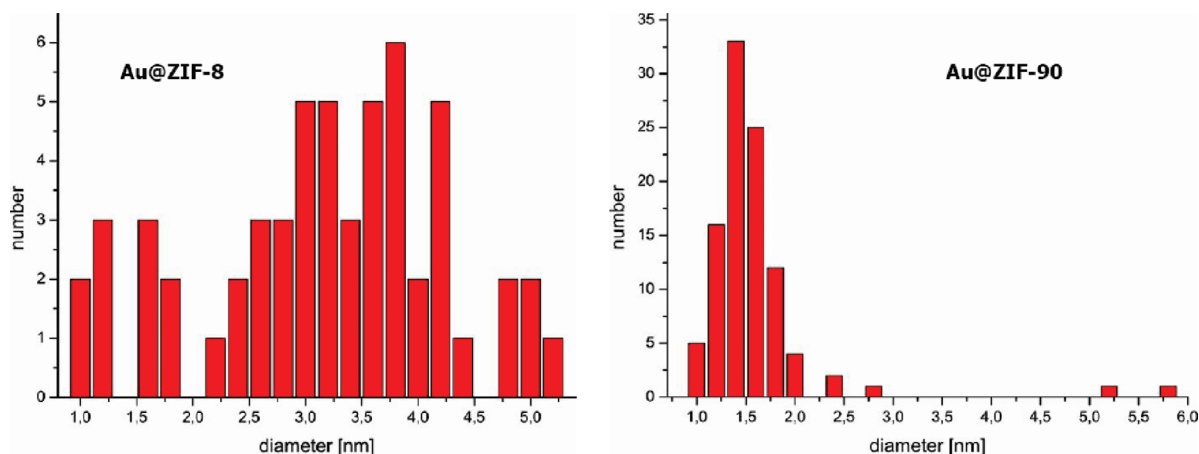


Figure 5. Size distributions of Au nanoparticles hosted inside ZIF-8 and ZIF-90 at the same loading level of 30 wt %. The aldehyde functionalized imidazolate linkers of ZIF-90 stabilize drastically smaller particles with a pronounced tendency matching with the cavity size of 1.2–1.3 nm.

Scheme 2. Schematic View of Liquid Phase Alcohol Oxidation with the Au@ZIF-8 material; Both Benzyl Alcohol (BA) and Methyl Benzoate (MB) Are Able to Access the Pores and Can Diffuse through the Network

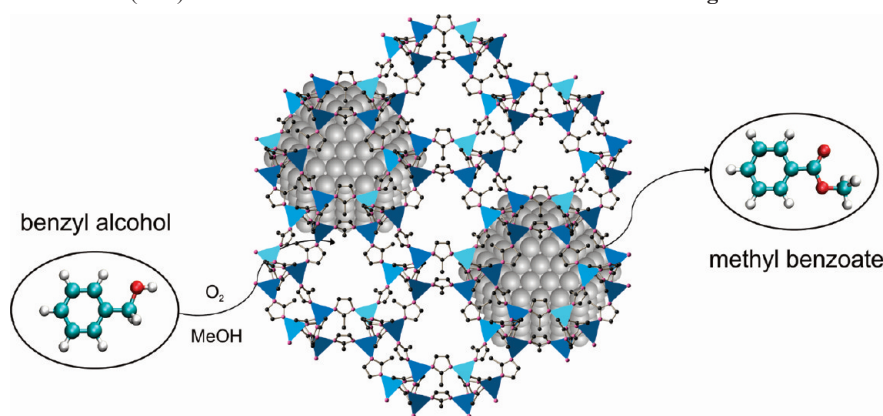


Table 2. Catalytic Activity of the Gold-Loaded ZIF Samples in Aerobic Oxidation of Benzyl Alcohol

catalyst	conversion (%)	selectivity (%)	yield (%)		
			PhCO ₂ Me	PhCHO	PhCH(OMe) ₂
none	0	0	0	0	0
ZIF-8	0	0	0	0	0
ZIF-90	0	0	0	0	0
Au@ZIF-8	81.2	98.2	79.74	1.46	0
Au@ZIF-90	12.74	50.55	6.44	6.3	0

Au@ZIF-90(ox) (**2-ox**) was prepared independently, i.e. without the simultaneous addition of BA. Therefore samples of Au@ZIF-90 (5, 15, and 30 wt %) were suspended in methanol and heated up to 80 °C under 5 bar oxygen. The oxidized materials Au@ZIF-90(ox) were fully characterized with PXRD, solid state NMR, FT-IR, UV–vis, and N₂ sorption measurements as described in detail in the Supporting Information. In case of Au@ZIF-90 not all, but a substantial fraction of aldehyde functions were converted and this fraction scales nicely with the level of Au loading. The relative intensity of the characteristic vibrations for the ester group was much lower in case of 5 wt % loading as compared with the 30 wt % loaded sample (Figure 6). This is as expected, because not all but only a fraction of the cavities are filled or affected by the loading with Au NPs (4.2% of the pores are filled).

The interaction of ester groups and/or carboxylic acid groups with the surface of the Au particles results in a characteristic absorption at 1608 cm^{−1} seen in the FT-IR spectra.

The catalytic and selective in situ oxidation of the ICA linkers in close proximity to the Au NPs inside ZIF-90 leads to sterically more demanding ester groups at the linkers which cause a downsizing of the pore aperture (Figure 7). Consequently the specific surface area drops further to 383 m² g^{−1} quite similar to the (non catalytic) postsynthetic functionalization of ZIF-90 to ZIF-92 (Zn(IIE)₂; IIE = imidazolate-2-iminoethanol) described by Yaghi et al.¹⁹ As a consequence of this post synthetic, catalytic functionalization of the aldehydes to yield alkylester groups the Au particles are not only stabilized but are likely to be encapsulated within the ZIF-90(ox) matrix.

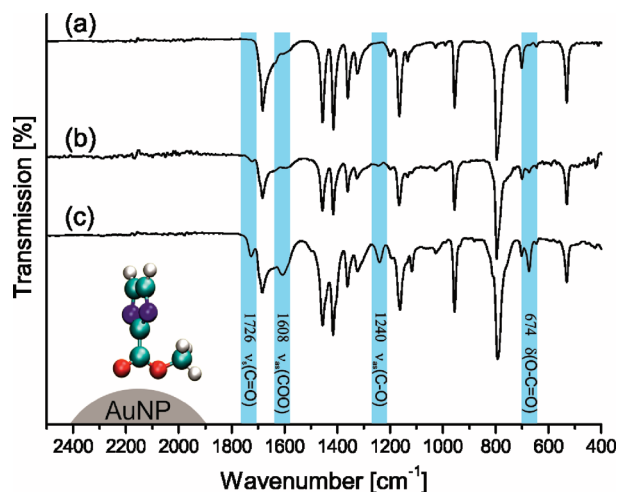


Figure 6. Detailed image of the fingerprint region of (a) activated ZIF-90, (b) Au_{5wt%}@ZIF-90(ox), and (c) Au_{30wt%}@ZIF-90(ox). The decrease in intensity of the absorption bands of imidazolate-2-methylcarboxylate (light blue) in Au_{5wt%}@ZIF-90(ox) is caused by the lower gold amount inside the framework, leading to a smaller number of ester groups. A molecular model of the IMC linker near to an Au NP points out the direct interaction of the linker molecules with the gold cluster, matching with the observed IR signal at 1608 cm⁻¹ (ν_{as}COO).²⁸

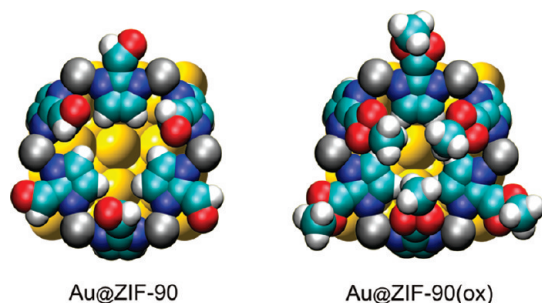


Figure 7. In situ oxidation of imidazolate-2-carboxyaldehyde groups of Au@ZIF-90 (**2**) leads to sterically more demanding ester groups at the linkers in proximity of the imbedded and catalytically active Au NPs. This causes a significant downsizing of the pore aperture around the particles of Au@ZIF-90(ox) (**2-ox**) leading to a reduction of the overall surface area. The schematic drawing is based on the structural parameters of ZIF-90 and the respective van der Waals radii.¹⁹

We suggest this site-selective encapsulation of small-cavity, size-matched Au particles by catalytic aerobic oxidation of the framework aldehyde groups as first example of a new concept of highly efficient stabilization of metal NPs against further growth inside the MOF matrix. This is evidenced by the PXRD patterns of the multiply loaded samples Au@ZIF-8, Au@ZIF-90 and Au@ZIF-90(ox) shown in Figure 8 in comparison to the singly loaded reference samples discussed above (Figure 1-6). Independent of the initial level of Au loading, the ZIF-8 and ZIF-90 frameworks totally collapse in the course of a second gas-phase loading by application of [Au(CO)Cl] and subsequent hydrogenation. This effect of pronounced instability of the MOF matrix during separate multiple loading with metal NPs was observed before for Pd@MOF samples prepared either by

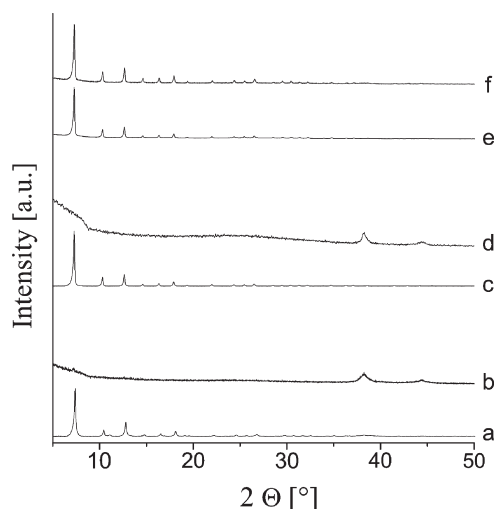


Figure 8. Comparison of the powder X-ray diffraction patterns of the one step and two step Au loading experiments: Au_{1.5wt%}@ZIF-8 (a) 1st and (b) 2nd loading; Au_{1.5wt%}@ZIF-90 (c) 1st and (d) 2nd loading; and Au_{1.5wt%}@ZIF-90(ox) (e) 1st and (f) 2nd loading. Note the characteristic X-ray diffraction peaks for larger Au nanoparticles of b and d. Only the Au@ZIF sample with encapsulated Au NPs (e) is stable during a second loading step (f).

gas-phase loading or by liquid phase impregnation.²⁹ It was assigned to catalytic decomposition of the metal precursors at the site of the pre-existing metal nanoparticles causing rapid particle growth which efficiently destroys the framework resulting in X-ray amorphous materials. Our data suggest a general effect independent from the type of metal, that is likely to ultimately limit metal loading of MOFs even in case of stabilizing groups at the linkers. In contrast, when the oxidized sample Au@ZIF-90(ox) (15 wt % Au) was treated a second time with [Au(CO)Cl] vapor, the ZIF matrix did not disintegrate at all and increased Au loadings of 30–40 wt % could be achieved without changing the typical Au particle size (Figure 3). The accessibility of the imbedded Au NPs of the various samples Au@ZIF for metal atoms was independently probed by alloying with mercury vapor at reduced pressure. The UV–vis surface plasmon resonance of the Au NPs was shifted indicating Au/Hg alloying, as expected, however with Au@ZIF-90(ox) as the remarkable exception of the series (see Figure S20c in the Supporting Information). Obviously, the encapsulated small Au NPs of Au@ZIF-90(ox) are no longer accessible, even for metal atoms. Neither [Au(CO)Cl] molecules nor Au atoms can reach the encapsulated Au NPs but are effectively trapped by the remaining not oxidized aldehyde groups of the framework rather than accessing the pre-existing Au NPs (Figure 7).

Conclusions

In conclusion, the selective formation, stabilization, and encapsulation of very small gold nanoparticles (Au NPs) homogeneously distributed throughout the crystalline matrix of zeolitic imidazolate frameworks (ZIFs) was achieved for the first time. It was shown how the network structure and especially the functional groups at the linkers influence the nanoparticle formation and control the size distribution and shape of the Au NPs and as well their surface accessibility.

(28) Wulandari, P.; Nagahiro, T.; Michioka, K.; Tamada, K.; Ishibashi, K.; Kimura, Y.; Niwano, M. *Chem. Lett.* **2008**, 37, 888–889.

(29) Esken, D.; Zhang, X.; Lebedev, O. I.; Schröder, F.; Fischer, R. A. *J. Mater. Chem.* **2009**, 19, 1314–1319.

Au@ZIF-8 show a high catalytic activity in the aerobic oxidation of benzyl alcohol in methanol and benzene, whereas the in situ oxidation of the aldehyde functions of Au@ZIF-90 leads to the encapsulation of the Au NPs inside the ZIF cavities. The directing effect of Lewis basic functionalized groups being present at the framework for anchoring metal nanoparticles inside MOF matrices was reported before.³⁰ However, we are going a step further presenting a new concept of loading MOFs with cavity size matching particles together with protecting the imbedded particles against further growth. We propose a general applicability of this concept to achieve a variety of metal@MOF materials of microstructure type C (Scheme 1) including multiple (subsequent) metal loading steps. Certainly, encapsulated metal particles will not be accessible as sites for catalytic transformations. However, this may be different for other applications of metal doped MOFs, for example, incorporating chemically inert magnetic nanoparticles. Last but not least, we like to suggest the perspective to fabricate novel MOF materials being loaded with NPs of different metals with or without alloying by developing a metal NP protection/deprotection methodology based on the site selective (auto)catalytic encapsulation of the primary formed metal nanoparticles as reported herein.

Experimental Section

Starting Materials. All chemicals were purchased from commercial suppliers (Sigma-Aldrich and STREM) and used without further purification. Manipulations were carried out under inert conditions using Schlenk-line and glovebox techniques (O_2 , H_2O , below 1 ppm). Solvents were purified, dried and saturated with Ar using an automatic catalytic Solvent Purification System (MBraun, Garching). The MOCVD precursor $[Au(CO)Cl]$ was purchased from STREM and stored at 8 °C under CO atmosphere.³¹ The pure ZIF-8 material $[(Zn(MeIM)_2)]_n$ was purchased from Sigma-Aldrich and activated at 300 °C under dynamic vacuum (1×10^{-3} mbar) for 24 h. ZIF-90 was derived following the procedure published by Yaghi et al.,¹⁹ scaled-up to yields of 1 g, activated at 1×10^{-3} mbar and 150 °C for 24 h. Characterization of the ZIF materials was done by FT-IR, PXRD, elemental analysis/AAS, solid-state NMR spectroscopy and thermo gravimetric analyses (TGA). The resulting analytical data and spectra fully agreed with published results. The surface areas were determined by N_2 sorption measurements and calculated with the BET model to 1918 $m^2 g^{-1}$ (ZIF-8) and 1664 $m^2 g^{-1}$ (ZIF-90). Further details are given in the Supporting Information.

Analytical Characterization. Elemental Analyses were performed in the Microanalytical Laboratory of the Department of Analytical Chemistry at the Ruhr-University Bochum. For metal determination (Zn, Au) an AAS apparatus by Vario of type 6 (1998) was employed, C, H, N analyses were carried out using a Vario CHNSO EL (1998) instrument. Infrared spectra were recorded inside a glovebox on a Bruker Alpha-P FT-IR instrument in the ATR geometry with a diamond ATR unit. UV-vis spectra were measured with a Perkin-Elmer Lambda 9 UV/vis/NIR spectrometer in diffuse reflectance mode using $BaSO_4$ as reference.

1H and ^{13}C -CP-MAS NMR-spectra were measured with a Bruker DSX, 400 MHz spectrometer under MAS conditions in 2.5 mm ZrO_2 rotors with a sample volume of 12 μL . The rotation frequency was 20 kHz. All spectra were measured applying pulse programs written by H.-J. Hauswald at the Department of Analytical Chemistry of the Ruhr-University Bochum. For the proton MAS NMR measurements a ZG4PM pulse program was used. The carbon NMR measurements were carried out with the pulse program CP4C (cross-polarization) and were referenced to adamantane at 38.56 ppm. Powder XRD (PXRD) measurements of the samples were recorded on a D8-Advance Bruker AXS diffractometer with $Cu K_{\alpha}$ -radiation ($\lambda = 1.5418 \text{ \AA}$) and a focused Göbel mirror in $\theta - 2\theta$ geometry with a position sensitive detector in a 2θ range from 5–90° at a scan speed of 10 s/step. Size of the gold nanoparticles was calculated via full profile analysis in Powder Cell 2.4 with the interpolated background and refining zero shift, and peak shape parameters for the pseudo-Voigt function. The experimental setup was in capillary mode. For data accumulation, the samples were filled under inert gas (glovebox) into 0.7 mm capillaries which were then sealed. N_2 sorption measurements were performed using a Quantachrome Autosorp-1 MP instrument and optimized protocols. Thermo gravimetric analyses (TGA) were performed on a Seiko TG/DTA 6300S11 instrument (sample weight approximately 10 mg) at a heating rate of 5 $K min^{-1}$ in a temperature range from 30–1000 °C. The measurement was performed at atmospheric pressure under flowing dinitrogen (99.9999%; flow rate = 300 $mL min^{-1}$).

Transmission Electron Microscopy (TEM). The measurements were carried out at the university of Antwerp, Belgium on a Philips CM20 microscope operating at 200 kV. High-resolution transmission electron microscopy experiments were performed on a JEOL 4000EX microscope operated at 400 kV with a point resolution of 1.7 Å. Electron tomography experiments were performed on a JEOL 300F TEM-STEM microscope operated at 300 kV and equipped with a -70° to $+70^\circ$ tomography tilt stage and holder. Images for tomographic reconstruction were taken using a 2 degree interval, over the largest possible angle (126° in this case). The tomographic reconstruction was obtained by weighted back projection using the TOM Tomography Toolbox³² and FEI Inspec 3D software packages. 3D visualization was performed using the AMIRA software, rendering the Au nanoparticles using an isosurface rendering and the ZIF matrices using a voltex rendering. For all techniques low intensity beam conditions (lowest possible magnification of between 50kx and 60kx for the BF tomography images, low beam intensities of $\sim 25 \text{ pA/cm}^2$ for BF imaging and $\sim 10 \text{ pA/cm}^2$ for diffraction patterns and long exposure times of 1–2 s for the BF images and 10–16 s for diffraction patterns) were used as much as possible to minimize the electron dose and possible beam damage of the nanoparticle supported framework.¹⁴ The images for the tomographic acquisition were taken in bright-field TEM instead of HAADF-STEM. Bright-field TEM needed to be used for the tomographic images (although unwanted diffraction contrast inevitably occurs with this technique), as prolonged STEM illumination damaged the samples. Animated 3D reconstruction showing the reconstructed Au particles rendered in gold and the ZIF-8 crystal rendered soft white. After a 360° rotation, the ZIF matrix is removed to view the particles clearly.

Au@ZIFs Preparation. Loading of ZIF-8 and ZIF-90 with the volatile metal precursor $[Au(CO)Cl]$ followed the general

(30) Hwang, Y. K.; Hong, D.-Y.; Chang, J.-S.; Jhung, S. H.; Seo, Y.-K.; Kim, J.; Vimont, A.; Daturi, M.; Serre, C.; Férey, G. *Angew. Chem., Int. Ed.* **2008**, *47*, 4144–4148.

(31) Belli Dell'Amico, D.; Calderazzo, F. *Inorg. Synth.* **1986**, *24*, 236–238.

(32) Nickell, S.; Förster, F.; Linaroudis, A.; Net, W. D.; Beck, F.; Hegerl, R.; Baumeister, W.; Plitzko, J. M. *J. Struct. Biol.* **2005**, *149*, 227–234.

(33) Hermes, S.; Schröder, F.; Amirjalayer, S.; Schmid, R.; Fischer, R. A. *J. Mater. Chem.* **2006**, *16*, 2464–2472.

procedure of loading metal–organic frameworks described in a previous publication.³³ Typical amounts of 100 mg ZIF material were placed together with the selected amount of the precursor, both contained in small glass vials, in a glass tube under CO atmosphere. Gas phase infiltration of [Au(CO)Cl] into ZIF-8 and ZIF-90 was performed in static vacuum (0.5 bar) at 60 °C for 72 h. After the loading procedure the tube was opened and the composite material was stored under CO atmosphere at –30 °C. The following reduction process of the precursor@ZIF samples was performed under hydrogen (2 bar) in a pressure jar at temperatures varying from 100 °C (Au@ZIF-8) to 130 °C (Au@ZIF-90). The new materials were characterized with FT-IR, UV–vis spectroscopy, PXRD, elemental analysis/AAS (Table 1), solid-state NMR spectroscopy, TGA, high-resolution and tomographic TEM measurements.

Catalytic Testing. A typical amount of 20 mg of Au@ZIF (10 wt % Au) was suspended in methanol, before 1 mmol benzyl alcohol (BA) were added. The reaction suspension was treated with 5 bar pure oxygen and heated up to 80 °C for 24 h, before solution was

filtered and analyzed with GC-MS techniques. Au@ZIF-8 exhibits a conversion of 81.2% with selectivity to methyl benzoate (MB) of 98.2%. The gold loaded ZIF-90 sample (Au@ZIF-90) shows a conversion of 13% and a selectivity of 50% (Table 2).

Acknowledgment. This work was supported by the German Research Foundation (DFG) within the Research Centre “Metal Support Interaction in Heterogeneous Catalysis” (SFB-558; fellowship for D.E.) and the Ruhr-University Research School. The authors acknowledge financial support from the European Union under the Framework 6 program under a contract for an Integrated Infrastructure Initiative. Reference 026019 ESTEEM. S.T. gratefully acknowledges the financial support from the Fund for Scientific Research Flanders (FWO).

Supporting Information Available: Additional figures (PDF) and 3D rendering (MPEG). This material is available free of charge via the Internet at <http://pubs.acs.org>.